Supporting Information:

Unveiling coordination transformation for dynamically enhanced hydrogen evolution catalysis

Liming Deng[a], Sung-Fu Hung[b], Sheng Zhao[a], Wen-Jing Zeng[b], Zih-Yi Lin[b], Feng Hu[a], Yaoyi Xie[a], Lijie Yin[a], Linlin Li[a], and Shengjie Peng[a]*

[a] College of Materials Science and Technology, Nanjing University of Aeronautics and Astronautics, Nanjing 210016, China. Email: pengshengjie@nuaa.edu.cn

[b] Department of Applied Chemistry, National Yang Ming Chiao Tung University, Hsinchu 300, Taiwan

Experimental section

Material synthesis

Materials:

All chemicals and materials were used as received without further purification. Cobalt nitrate hexahydrate ($Co(NO_3)_2 \cdot 6H_2O$, 99%), sodium borohydride ($NaBH_4$, 96%), potassium hydroxide (KOH, 99%), Ti_3AlC_2 powders (200 mesh), lithium fluoride (LiF, 99%), hydrochloric acid (HCl), sodium carbonate (Na_2CO_3, 99%), sodium tungstate ($Na_2WO_4 \cdot 2H_2O$, 99%) and platinum on graphitized carbon (Pt/C, 20 wt%) were purchased from Macklin.

Preparation of $Ti_3C_2T_x$ MXene nanosheets:

$Ti_3C_2T_x$ MXene was synthesized by selective etching Al from Ti_3AlC_2 using in situ HF-forming etchants. The etching solution was prepared by adding 2.0 g of LiF into 30 mL of 9 M HCl, followed by stirring for 5 min. Then, 2.0 g of Ti_3AlC_2 powder was slowly added into the above solution at 45 °C and stirred for 36 h. Subsequently, the acidic mixed solution containing MXene was washed with distilled water several times by centrifugation (4500 rpm) until the supernatant reached neutral pH (d > 6). Finally, the obtained powders were dispersed in 250 mL of distilled water and sonicated for 2 h under Ar flow, followed by centrifuging for 1 h at 3500 rpm. The resultant supernatant was decanted and collected. (MXene dispersion content $\approx$ 3 mg mL^{-1}).

Preparation of CoB_i/MXene and CoB_i:

In order to obtain MXene nanosheets that have metal ions adsorbed onto them, a solution was prepared by dissolving 30 mL of MXene dispersion (3 mg mL^{-1}) and 10 mmol of $Co(NO_3)_2 \cdot 6H_2O$ in N_2-saturated deionized water (DI, 30 mL). This solution was designated as solution A. Solution B was prepared by dissolving 10 mmol of $NaBH_4$ in N_2-saturated DI water under an ice bath. Solution B was added dropwise to solution A while stirring in an ice bath, and the resulting mixture was allowed to stand for 1 h. The formed precipitate, CoB_i/MXene, was washed with DI water and then vacuum-dried at 60

°C for 6 h. As a comparison, individual CoB_i was prepared as a counterpart. To obtain CoB_i, the excess $NaBH_4$ solution was directly added to an N_2-saturated mixed solution of $Co(NO_3)_2 \cdot 6H_2O$ in an ice bath. The precipitate was also washed and dried as before.

Preparation of CoC_i/MXene and CoW_i/MXene:

To prepare CoC_i/MXene, a solution denoted as A was obtained by dissolving 10 mmol of Na_2CO_3 in 30 mL of DI. Next, 10 mmol of $Co(NO_3)_2 \cdot 6H_2O$ was dissolved in a mixture of 30 mL of MXene and 30 mL of DI water saturated with N_2, resulting in a solution referred to as B. Solution B was then gradually added dropwise to solution A and stirred at room temperature for 6 h. Subsequently, the dispersion was collected through centrifugation, washed, and dried. The same procedure was followed to prepare CoW_i/MXene, but Na_2CO_3 was replaced with Na_2WO_4.

Fabrication of Pt/C at Ni foam:

An immobilization ink solution was firstly prepared by mixing 10 mg Pt/C with 40 μL Nafion, then dispersed in 1.0 mL of water-ethanol solution ($V_{Water}/V_{Ethanol} = 4{:}1$), followed by 40 min sonication. A piece of the treated Ni foam was then immersed into the ink solution for 1 min and dried in air at room temperature. Such a loading treatment process was repeated for 3 times to obtain Pt/C work electrode with a Pt/C mass loading of ~1.5 mg cm^{-2}.

Material Characterizations

Observations of the morphologies and microstructures of various materials were conducted using SEM (Regulus 8100), TEM, and HRTEM (FEI Tecnai G2 F20). The crystal structures of electrocatalysts were examined using XRD (Bruker D8). To determine the surface composition of the catalysts, measurements were taken with Al Kα X-rays utilizing XPS (Escalab 250Xi electron spectrometer). The BET-specific surface area was obtained by conducting N_2 adsorption-desorption tests using the V-Sorb 2008P instrument. X The XANES and EXAFS measurements were conducted at the Taiwan Photon Source (TPS) beamline, 44A Quick-scanning XAS, located at the National

Synchrotron Radiation Research Center (NSRRC) in Hsinchu, Taiwan. The in-situ Raman spectra were collected utilizing RENISHAW instrumentation, with an excitation wavelength of 633 nm.

A specialized acrylic container with a 1-millimeter gap was designed and sealed using Kepton tape to perform in-situ XRD measurements under conditions similar to those utilized during electrochemical characterization. The sample and electrolyte were then subjected to 16 keV of incident X-rays transmitted perpendicular to the surface, with the signal from the resulting synchrotron X-ray diffraction collected through the use of a large Debye-Scherrer camera located at BL-01C2 within the NSRRC in Taiwan. The XRD patterns were calibrated against a CeO_2 standard and calibrated to a wavelength of 1.5418 Å using Winplotr.

In-situ X-ray absorption spectroscopy, including XANES and EXAFS at Co K-edge, were collected in total-fluorescence-yield mode using a silicon drift detector in BL-44A at National Synchrotron Radiation Research Center (NSRRC), Taiwan. The measurement in a typical three-electrode setup as the same condition in the electrochemical characterization case was performed in a specially designed Teflon container with a window sealed by Kempton tape. The scan range was kept in an energy range of 7600-8300 eV for Co K-edge. Subtracting the baseline of pre-edge and normalizing that of post-edge obtained the spectra. EXAFS analysis was conducted using Fourier transform on k^2-weighted EXAFS oscillations. All EXAFS spectra are presented without phase correction.

Electrochemical measurements

The electrochemical measurements were carried out in a three-electrode system utilizing an Autolab PGSTAT302 in a 1 M KOH electrolyte. The working electrode was fabricated by mixing the obtained catalyst with a conductive agent (carbon black) and binder (Polyvinylidene fluoride, PVDF) in a mass ratio of 7:2:1 to obtain a catalyst slurry. The slurry was subsequently coated on a 1×1 cm^2 nickel foam substrate and dried at 60 °C

under vacuum for 12 h, resulting in a loading mass of approximately 1.5 mg cm^{-2}. A graphite rod was used as the counter electrode (CE), while Ag/AgCl (Saturated KCl) electrode was employed as the reference electrode (RE). All potentials were converted to the reversible hydrogen electrode (RHE) scale by applying the Nernst equation (E_{RHE} = $E_{Ag/AgCl}$ + 0.198 + 0.0591 × pH). Linear sweep voltammetry (LSV) curves were recorded at a scan rate of 5 mV s^{-1}, and *iR* compensation was applied. The ECSA was calculated from non-Faraday regions of the cyclic voltammetry (CV) curves obtained at different scan rates. EIS was performed with a frequency range of 0.1-10^5 Hz and an amplitude of 5 mV.

Computational Methods

To conduct the DFT calculations within the generalized gradient approximation (GGA) using the Perdew-Burke-Ernzerhof (PBE) formulation, the Vienna Ab Initio Package (VASP) was utilized. The ionic cores were described using projected enhanced wave (PAW) potentials, and valence electrons were taken into account using a plane-wave basis set with a kinetic energy cutoff of 450 eV. The Gaussian smearing method with a width of 0.05 eV was employed to allow for partial occupancies of the Kohn-Sham orbitals. The electronic energy was considered self-consistent when the energy change was less than 10^{-4} eV, and a geometry optimization was deemed convergent when the force change was less than 0.05 eV Å^{-1}. Dispersion interactions were described using Grimme's DFT-D3 methodology, and the Brillouin zone integral used the surface structures of a 1×1×1 Monkhorst-Pack K-point sampling. The free energies (ΔG) of basic reaction steps were calculated as $\Delta G = \Delta E + \Delta E_{ZPE} - T\Delta S$, where ΔE is the difference in total energy, ΔE_{ZPE} and ΔS represent the differences in zero-point energy and entropy variation, and T denotes the temperature (set to 300 K here).

Supplementary Fig.s
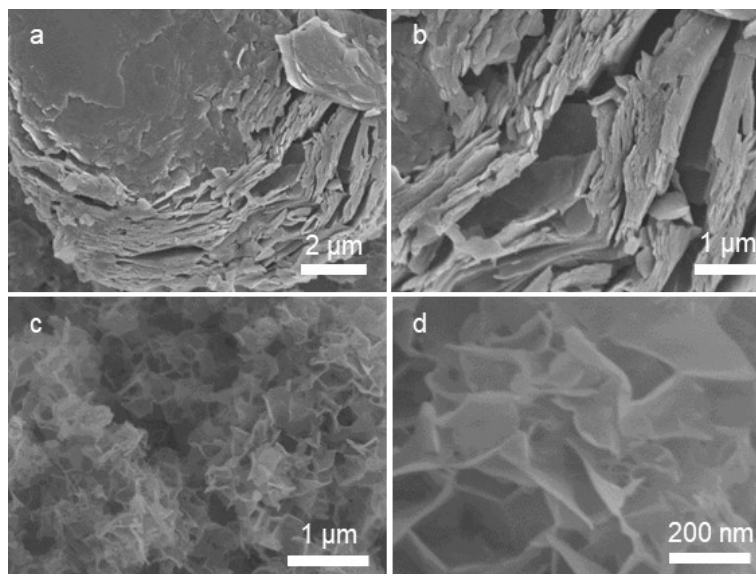
Fig. S1. SEM images of (a and b) accordion-like MXene $Ti_3C_2T_x$. (c and d) SEM images of bare CoB_i at different magnifications.

The HF-etched $Ti_3C_2T_x$ presents an accordion-like multilayer structure. From the SEM image of CoB_i, it can be observed that they are smooth and uniform with a micron-sized planar area.
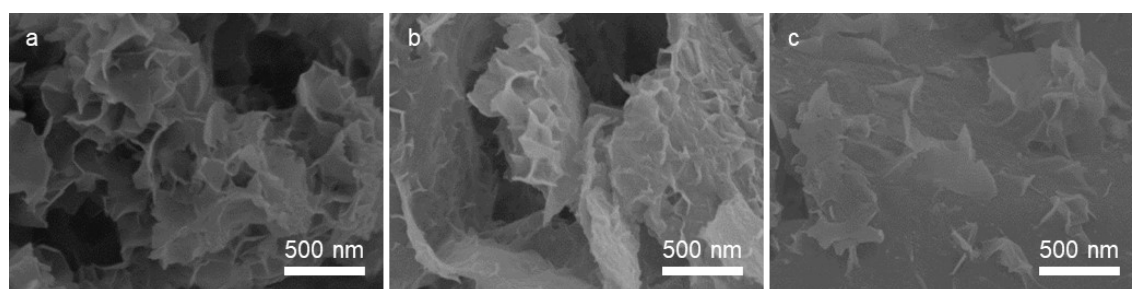
Fig. S2. SEM images of CoBi/MXene with different ratios (a) CoB_i/Mxene-10; (b) CoB_i/Mxene-30; (c) CoB_i/Mxene-50.

CoB_i/MXene hybrids with different addition portions of MXene solution show no significant morphology change.
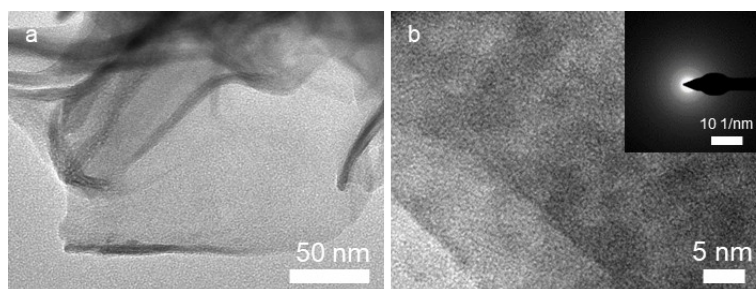
Fig. S3. (a) TEM and (b) HRTEM images of the CoB_i nanosheets.
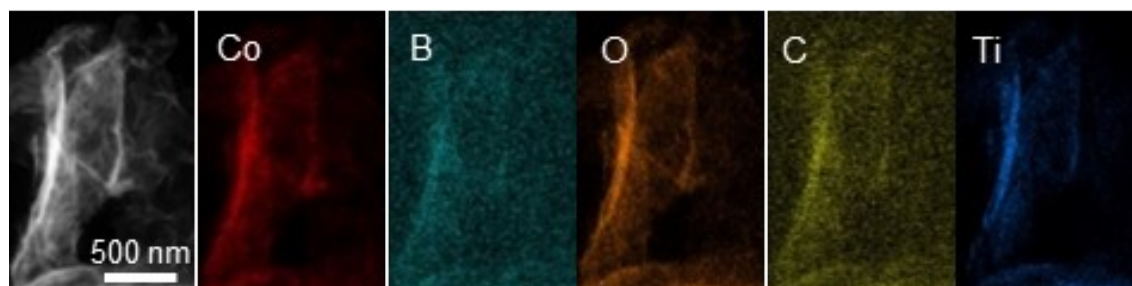
Fig. S4. HADDF-STEM image and corresponding elemental mappings of CoB_i/MXene.

The uniform distribution of Co, B, Ti, O, and C elements in CoB_i/MXene nanohybrids was visualized by elemental mapping analysis.
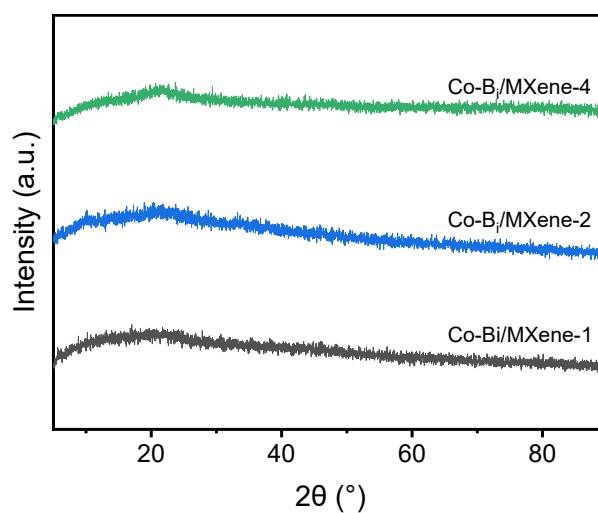
Fig. S5. XRD patterns of CoB_i/MXene with different ratios.

The absence of peaks in the XRD pattern suggests that CoB_i/MXene hybrids with different amounts of MXene are amorphous.
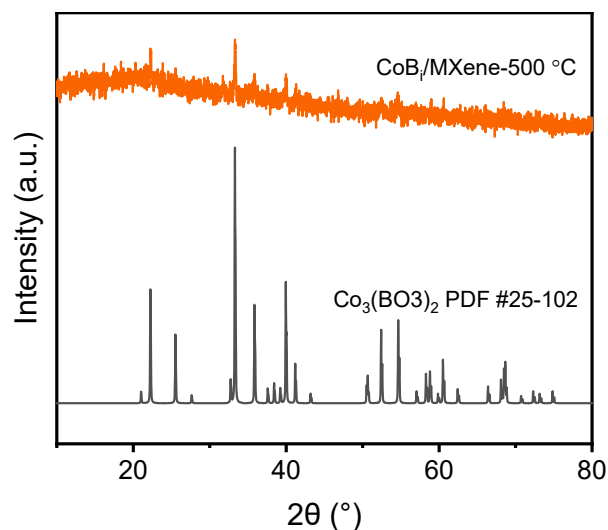
Fig. S6. XRD patterns of CoB_i/MXene-500°C.

The material crystallinity can be enhanced by annealing to confirm its composition. In the XRD pattern of CoB_i/MXene-500°C, the diffraction peak are well-matched with $Co_3(BO_3)_2$ (PDF #25-102), indicating that CoB_i/MXene is a composite of amorphous $Co_3(BO_3)_2$ and MXene.
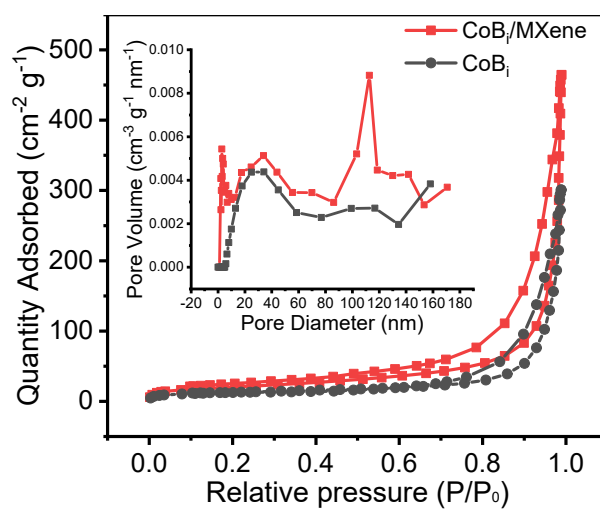
Fig. S7. The pore size distribution diagram and N_2 adsorption and desorption curve of CoB_i and CoB_i/MXene.
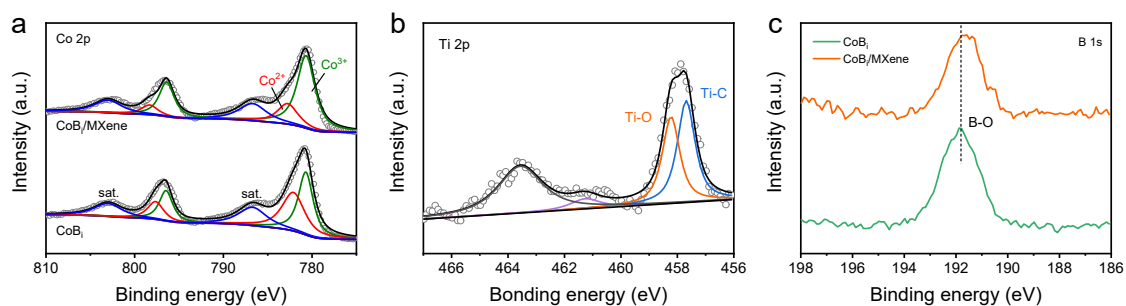
Fig. S8. High-resolution XPS spectra of (a) Co 2p, (b) Ti 2p, and (c) B 1s.
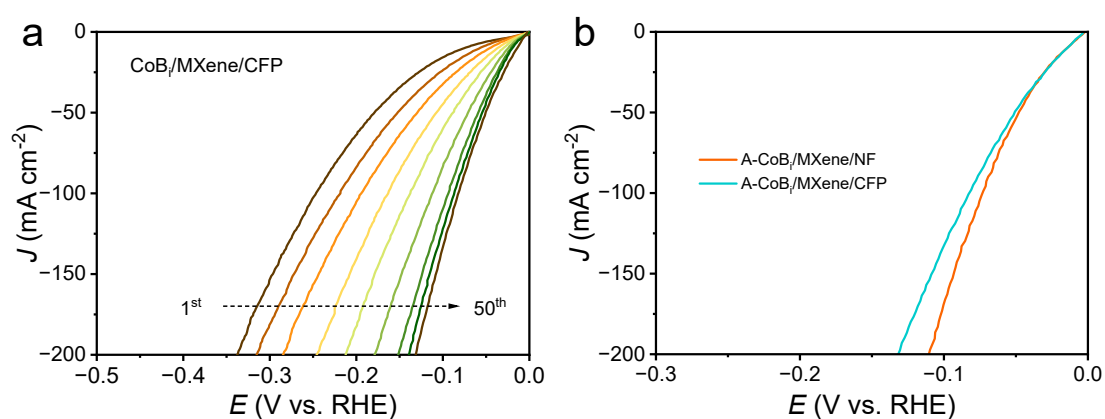
Fig. S9. (a) Polarization curves corresponding to different LSV scans of CoB$_i$/MXene on the CFP substrate. (b) Performance comparison of catalyst A-CoB$_i$/MXene on nickel foam (NF) and carbon fiber paper (CFP) substrates.
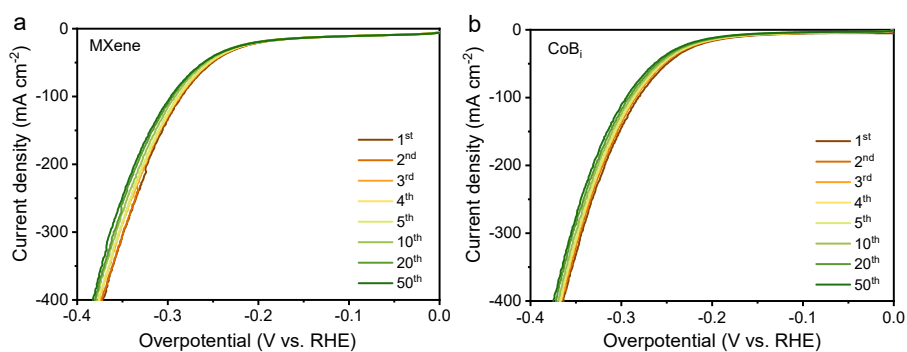
Fig. S10. Consecutive LSV curves of HER for (a) MXene and (b) CoB$_i$.
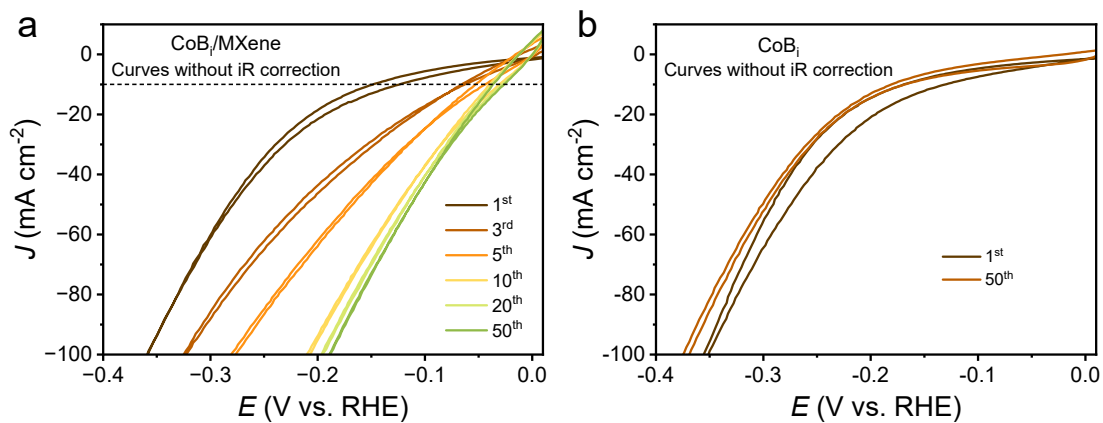
Fig. S11. Complete LSV curves of (a) CoB_i/MXene and (b) CoB_i during the activation process with the scan rate of 50 mV s^{-1}.
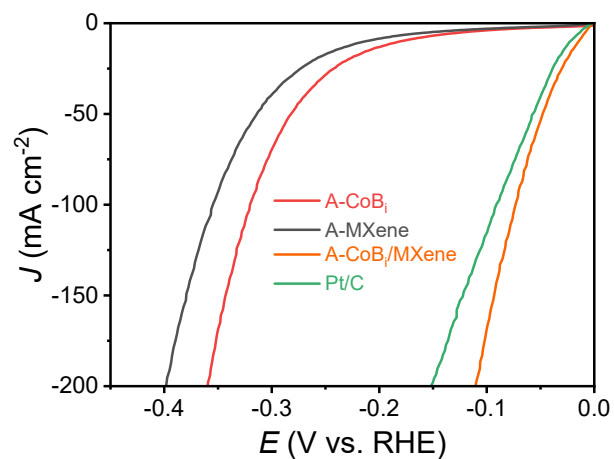
Fig. S12. LSV curves of A-MXene, A-CoB_i, and A-CoB_i/MXene in comparison with commercial Pt/C in the range of 0~200 mA cm^{-2}.
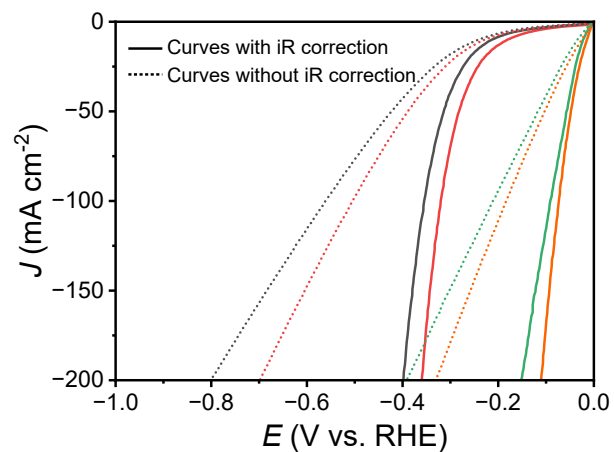
Fig. S13. LSV curves of different electrodes before and after iR correction in 1.0 M KOH.
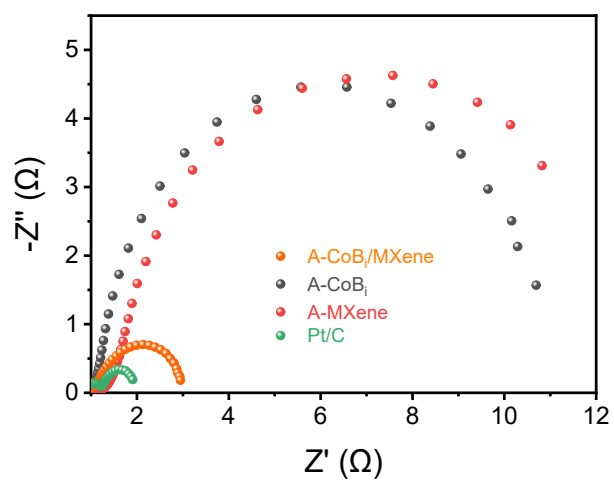
Fig. S14. EIS curves of A-MXene, A-CoB$_i$, A-CoB$_i$/MXene, and Pt/C, respectively.
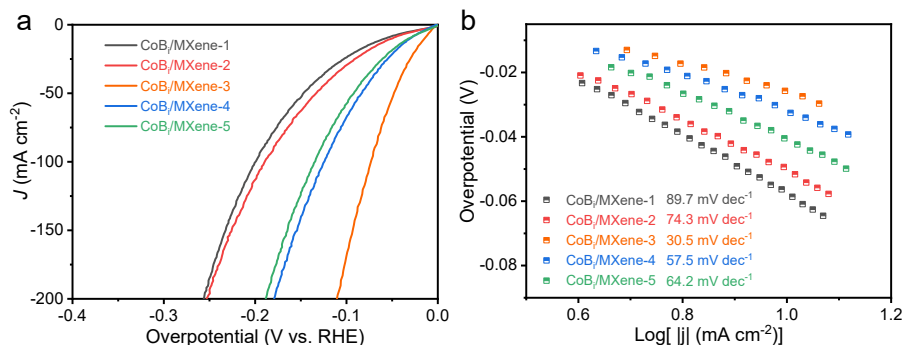
Fig. S15. (a) HER Polarization curves, (b) Tafel slope of CoB$_i$/MXene with different ratios.

CoB$_i$/MXene exhibited the best HER electrocatalytic performance compared to other catalysts with different amounts of MXene.
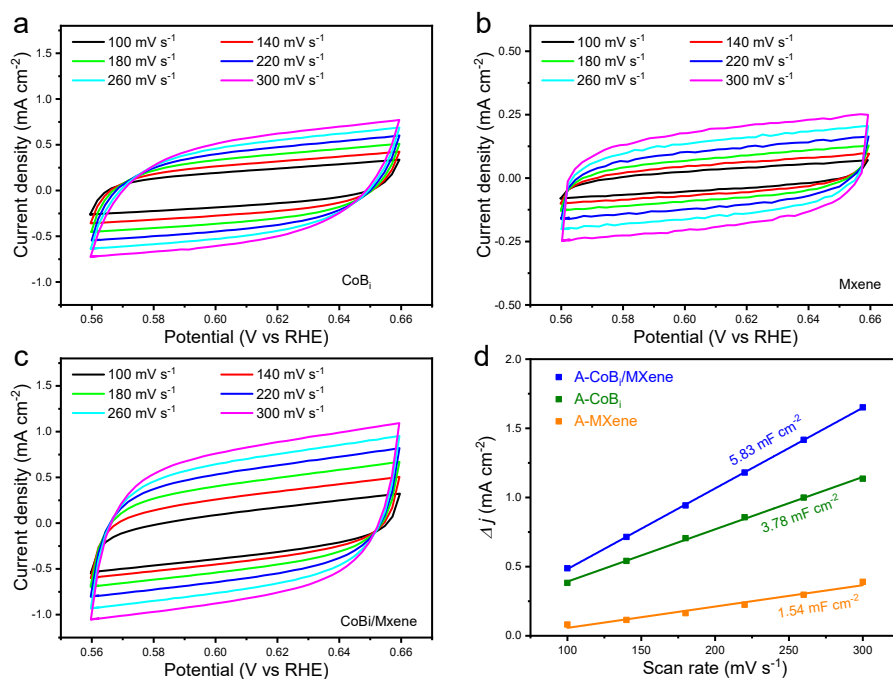
Fig. S16. (a-c) CV of A-MXene, A-CoB$_i$, and A-CoB$_i$/MXene at different scan rates in the voltage range of 0.56 to 0.66 V, respectively; (d) Double-layer capacitance (C$_{dl}$) of A-MXene, A-CoB$_i$, and A-CoB$_i$/MXene (where ΔJ is the difference between anodic and cathodic current densities in CV curves at different scan rates in a non-Faradaic region).

The value of C$_{dl}$ was calculated to evaluate the electrochemical surface area (ECSA).
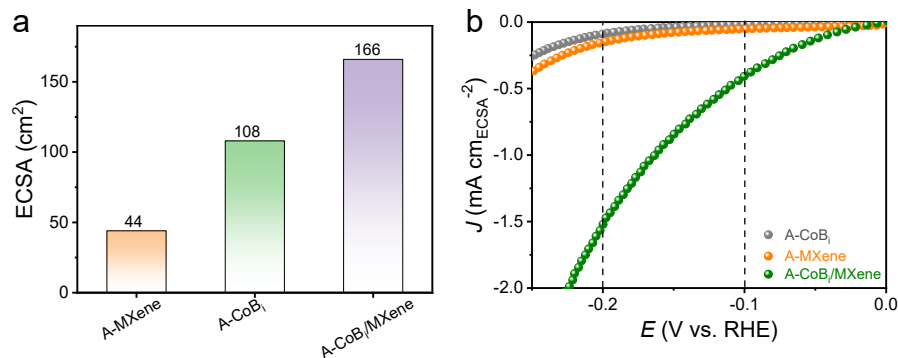
Fig. S17. (a) ECSA values of A-MXene, A-CoB$_i$, and A-CoB$_i$/MXene. (b) HER polarization curves normalized by ECSA.
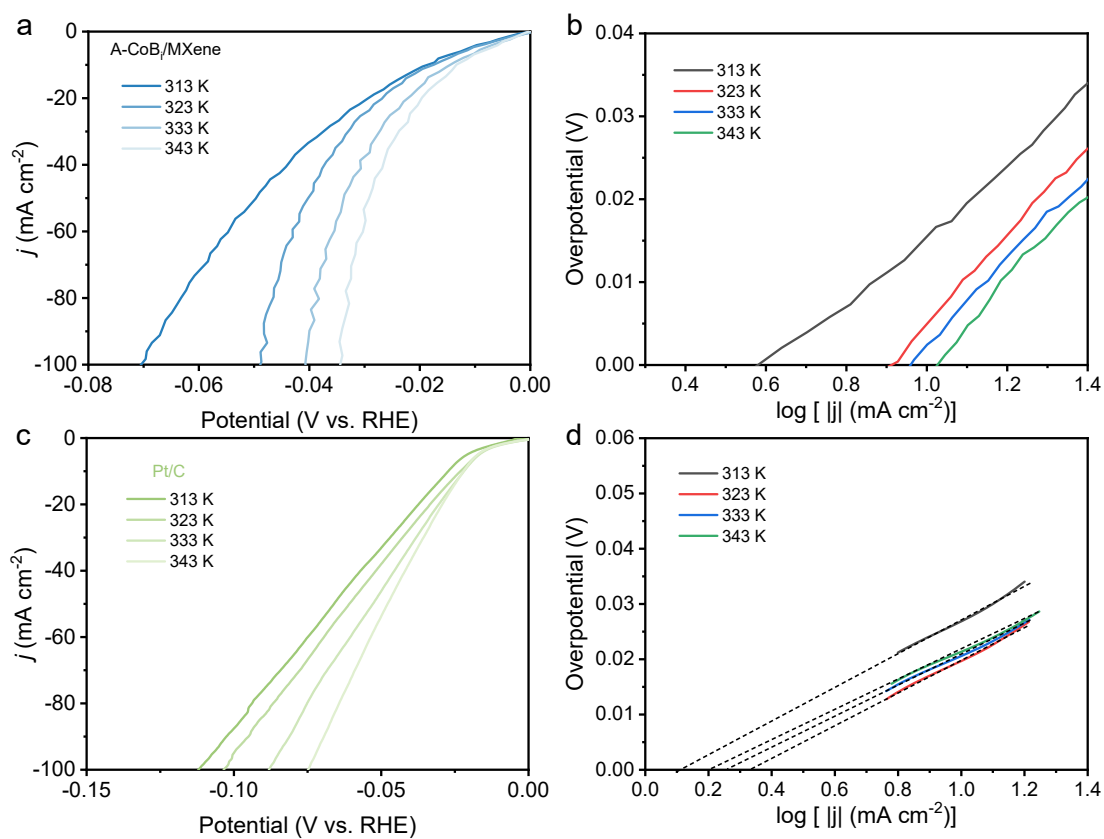
Fig. S18. LSV polarization curves with 85% iR correction and Tafel plots of (a and b) A-CoB$_i$/MXene and (c and d) commercial Pt/C catalysts measured at different temperatures ranging from 313 to 343 K in 1 M KOH solution.
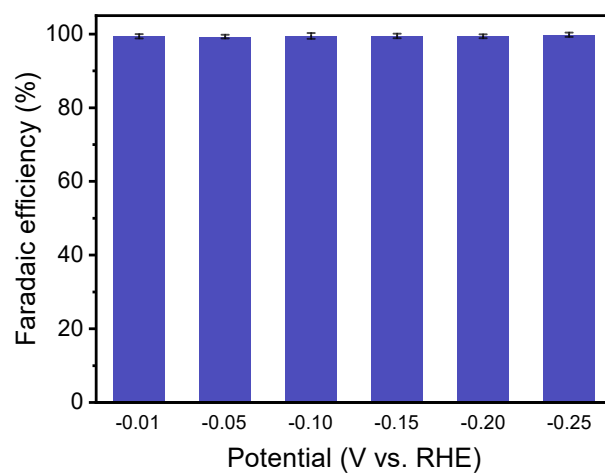
Fig. S19. The detected and theoretical volume of H_2 generated in a potentiostatic experiment.
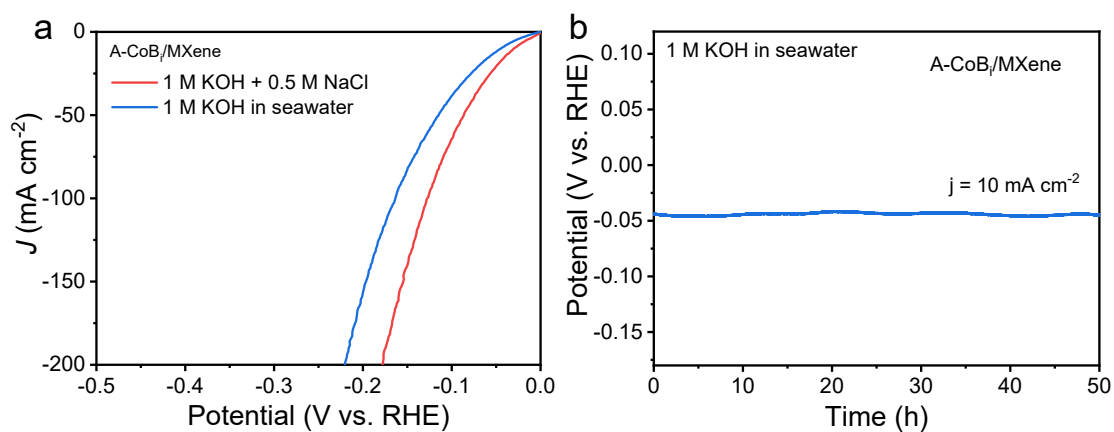
Fig. S20. (a) HER polarization curves of A-CoB$_i$/MXene in different electrolytes. (b) Chronopotentiometry curve of A-CoB$_i$/MXene in 1 M KOH seawater electrolytes.
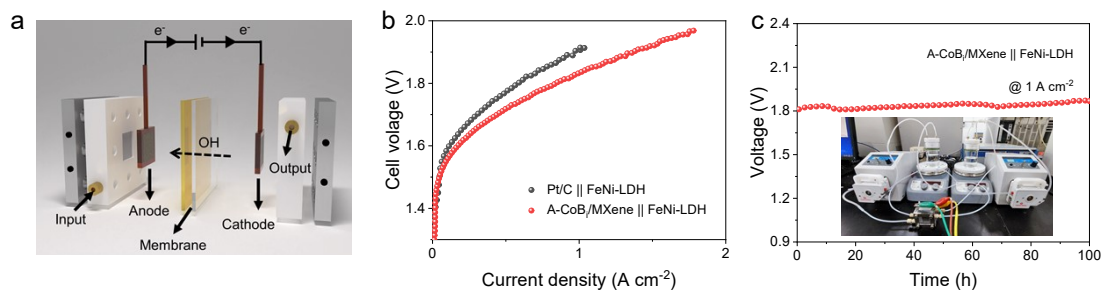
Fig. S21. (a) Schematic of the two-electrode AEM electrolyzer devices using Pt/C or A-CoB$_i$/MXene and NiFe LDH as cathode and anode. (b) Polarization curves for overall water splitting of the devices with Pt/C or A-CoB$_i$/MXene and NiFe LDH electrodes. (c) Chronopotentiometric curve of the device with a A-CoB$_i$/MXene electrode in 1 M KOH electrolyte.
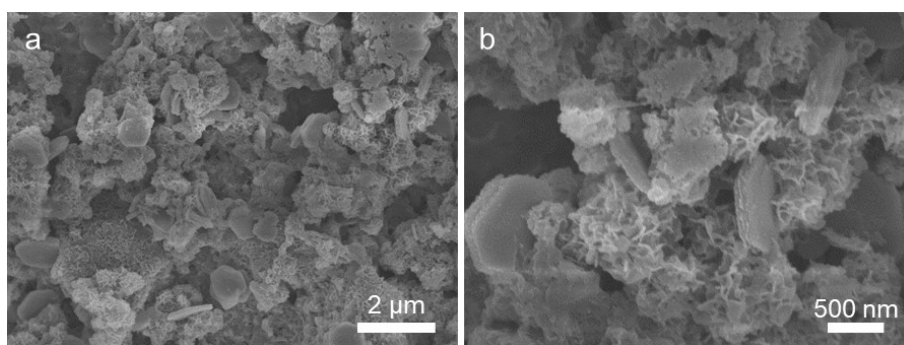
Fig. S22. SEM images of (a and b) CoB$_i$/MXene-10th.
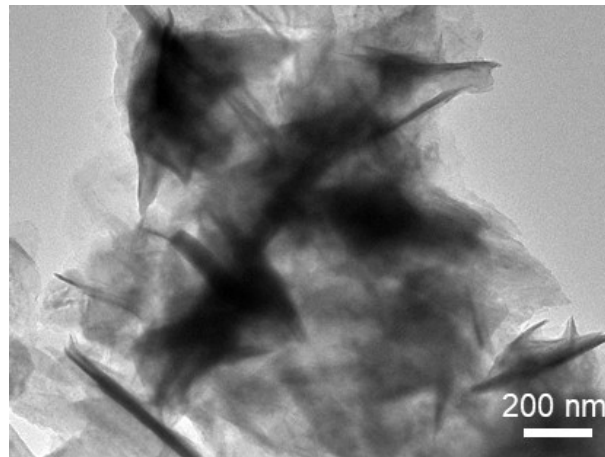
Fig. S23. TEM images of A-CoB$_i$/MXene.
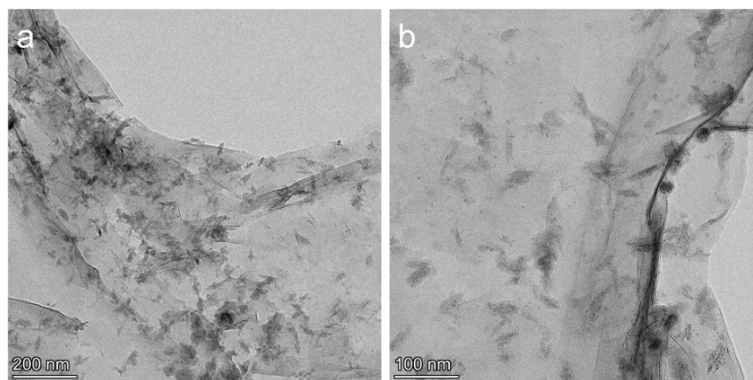
Fig. S24. (a) Low-magnified and (b) high-magnified TEM images of MXene, respectively.
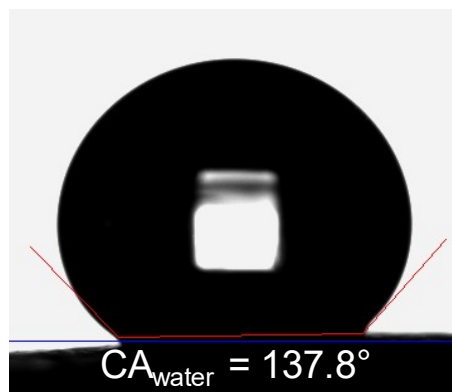
Fig. S25. The photo of the contact angle of CoB$_i$.
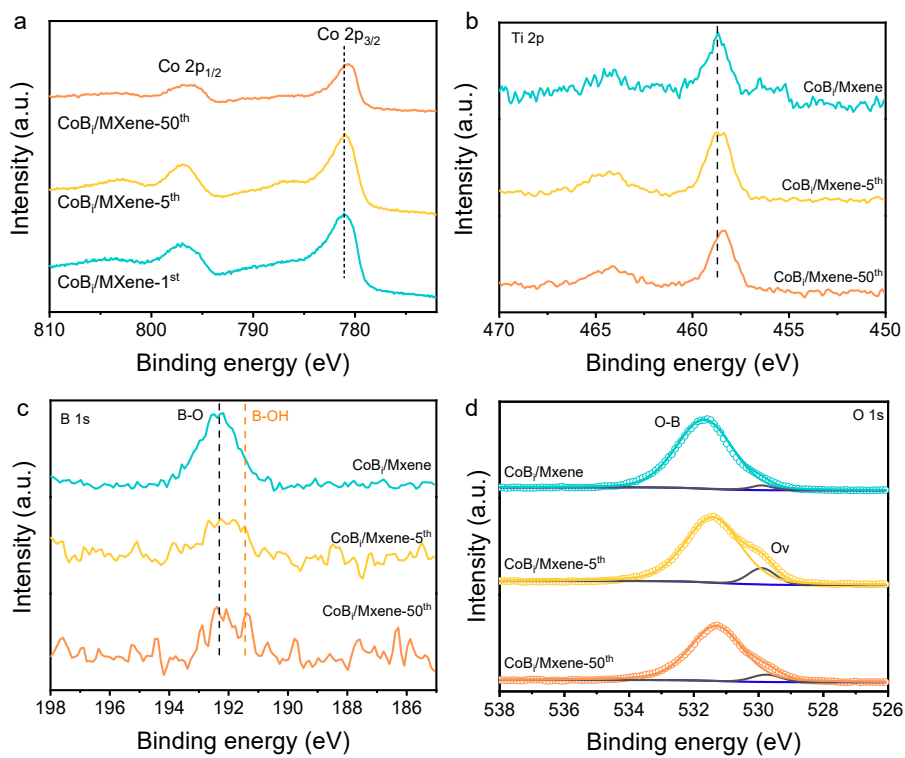
Fig. S26. Comparison of the (a) Co 2p, (b) Ti 2p, (c) B 1s, (d) O 1s XPS spectra before and after activation of CoB$_i$/MXene.
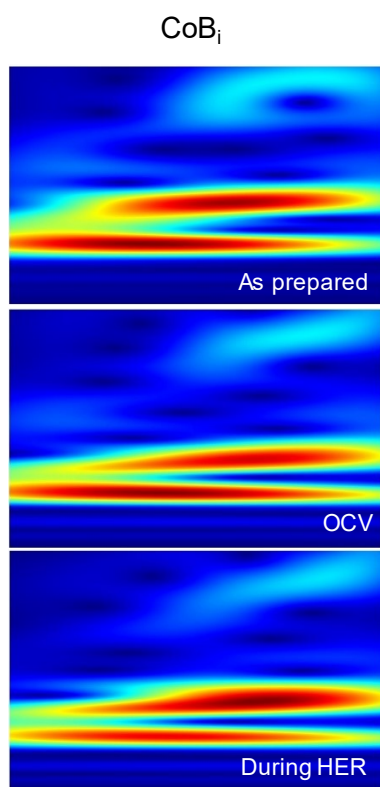
CoB$_i$

Fig. S27. WT-EXAFS of CoB$_i$ at different stages of reaction.
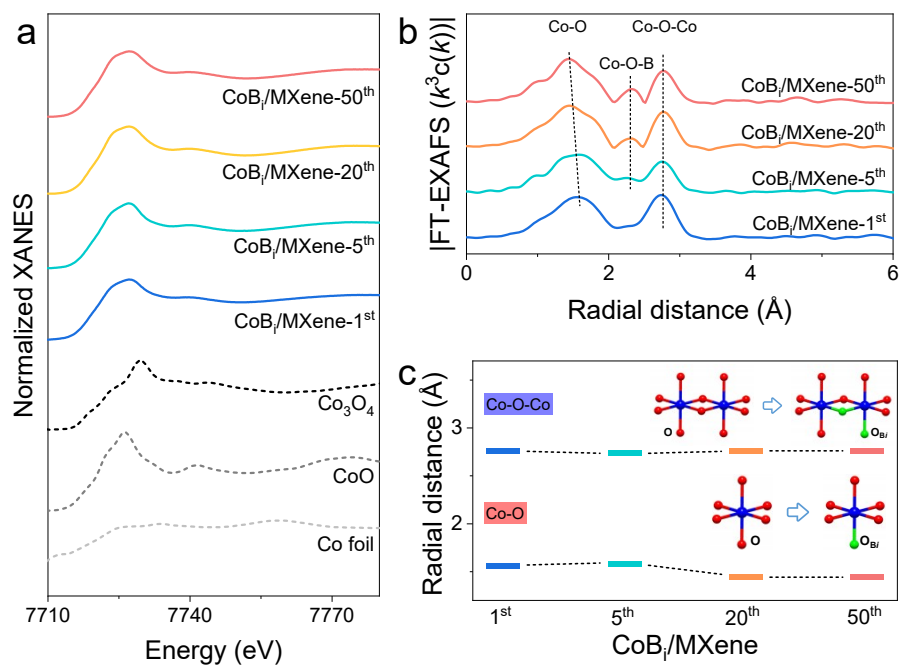
Fig. S28. (a and b) XANES and FT-EXAFS spectra of the CoB$_i$/MXene electrode after different cycles. (c) The radial distance of the Co–O shell and the Co–Co shell for CoB$_i$/MXene.
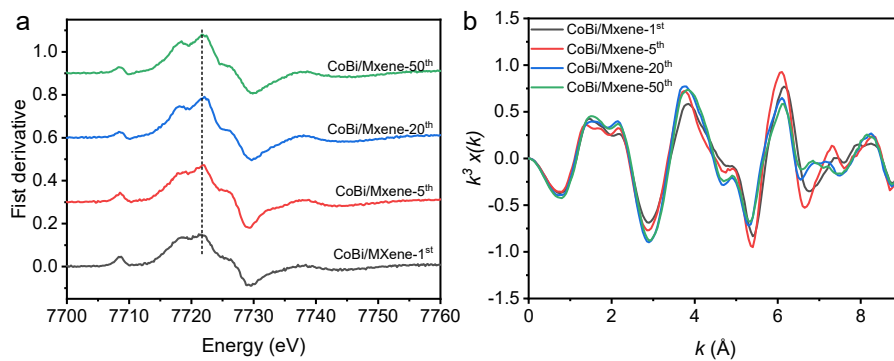
Fig. S29. (a) First derivative curves (b) Co K-edge EXAFS oscillation function of CoB$_i$/MXene-1st, CoB$_i$/MXene-5th, CoB$_i$/MXene-20th, and CoB$_i$/MXene-50th.
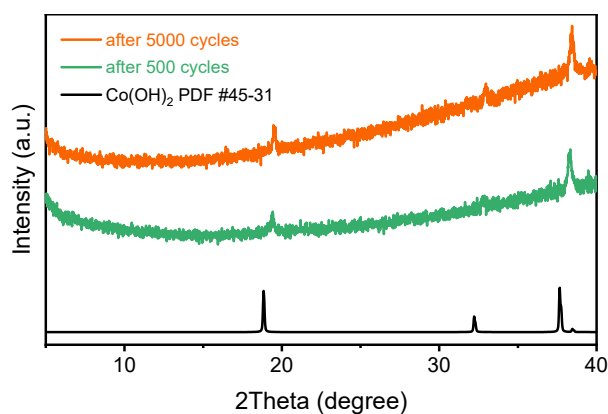
Fig. S30. XRD patterns of CoB$_i$/MXene before and after long-term stability testing in 1 M KOH.

After long-term stability testing, the XRD results indicated that the Co(OH)$_2$ phase was continuously retained.
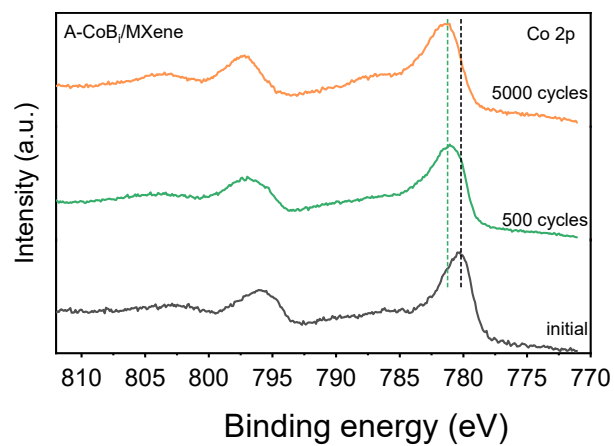
Fig. S31. Co 2p for CoB$_i$/MXene after the HER stability test.
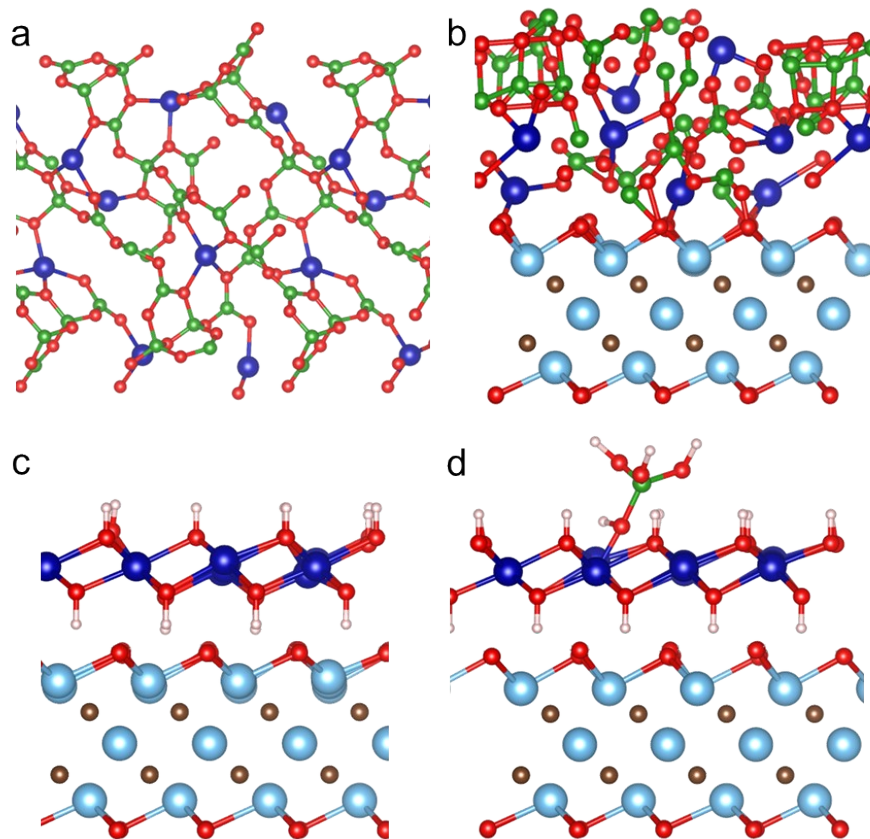
Fig. S32. The DFT Calculated structural models for (a) CoB$_i$, (b) CoB$_i$/MXene, (c) Co(OH)$_2$/MXene, (d) B$_i$-Co(OH)$_2$/MXene.
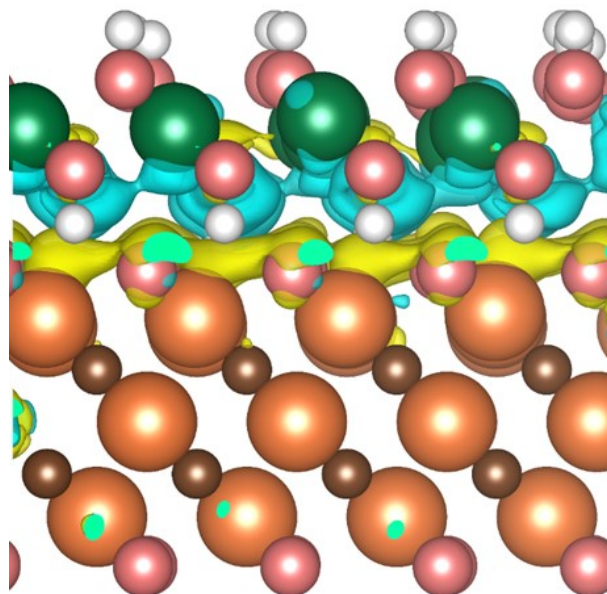
Fig. S33. Charge density difference of Co(OH)$_2$/MXene.
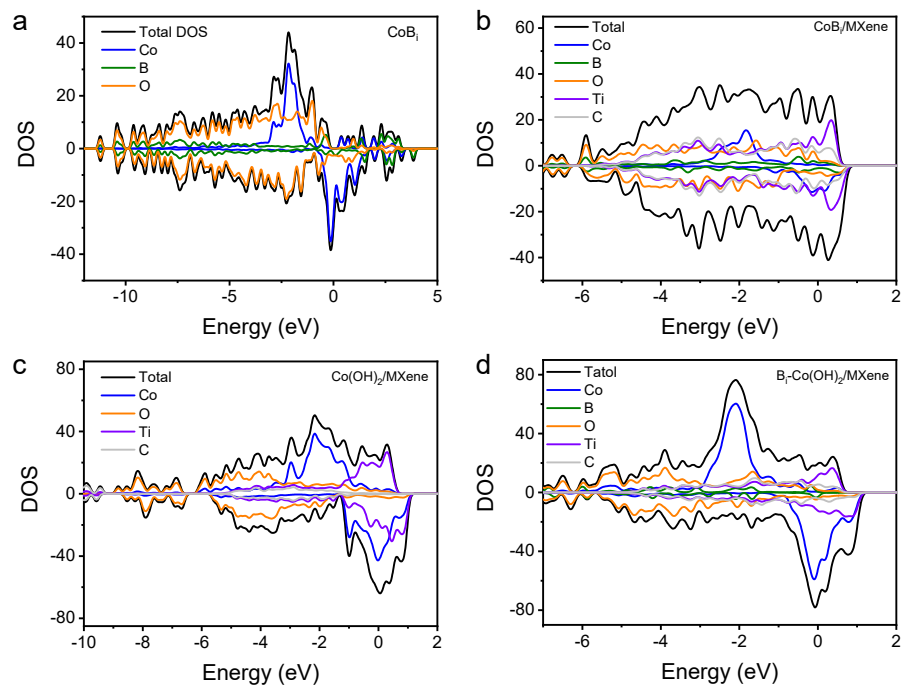
Fig. S34. The projected density of states (PDOS) of (a) CoB_i, (b) CoB_i/MXene, (c) $Co(OH)_2$/MXene, (d) B_i-$Co(OH)_2$/MXene.

The projected density of state (PDOS) suggests that the local density of state at the Fermi level of Co 3d orbital increases with the coordination of the $B(OH)_4$, which boosts the catalytic activity.
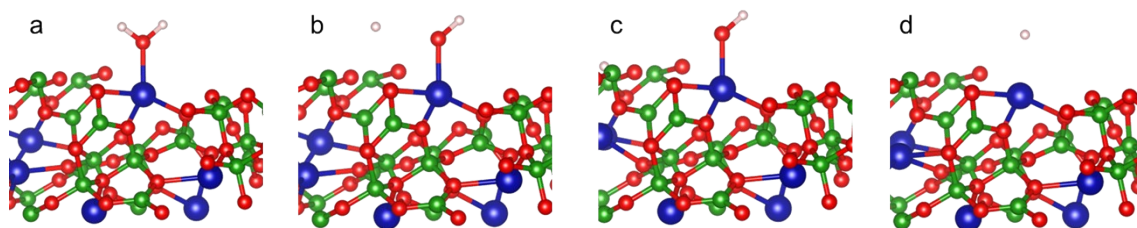
Fig. S35. Chemisorption models of (a) H_2O, (b) H and OH, (c) OH, and (d) H on the CoB_i.
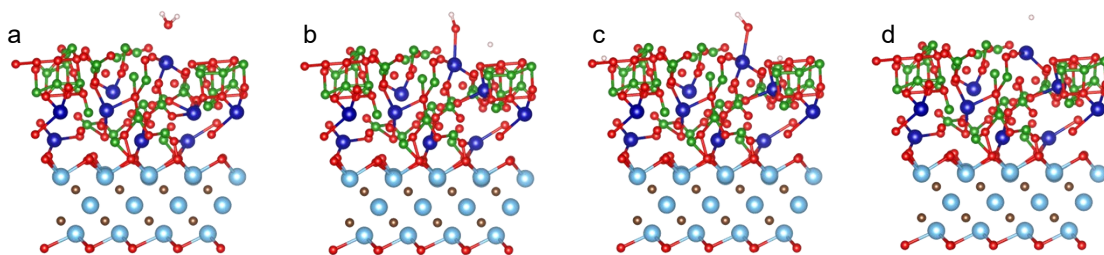
Fig. S36. Chemisorption models of (a) H$_2$O, (b) H and OH, (c) OH, and (d) H on the CoB$_i$/MXene.
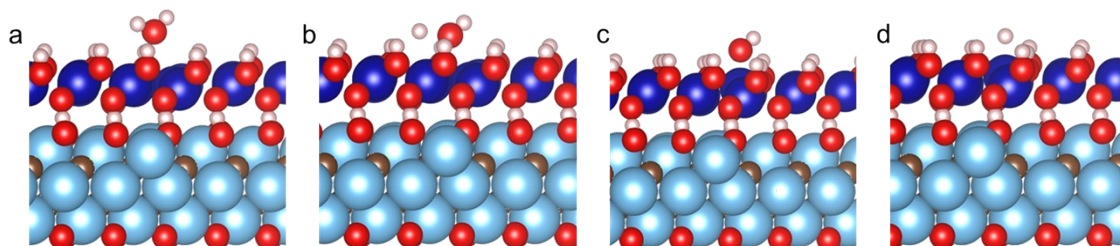
Fig. S37. Chemisorption models of (a) H$_2$O, (b) H and OH, (c) OH, and (d) H on the Co(OH)$_2$/MXene.
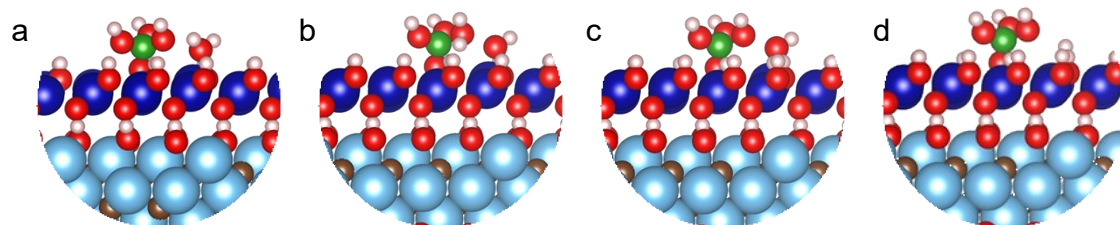
Fig. S38. Chemisorption models of (a) H$_2$O, (b) H and OH, (c) OH, and (d) H on the B$_i$-Co(OH)$_2$/MXene.
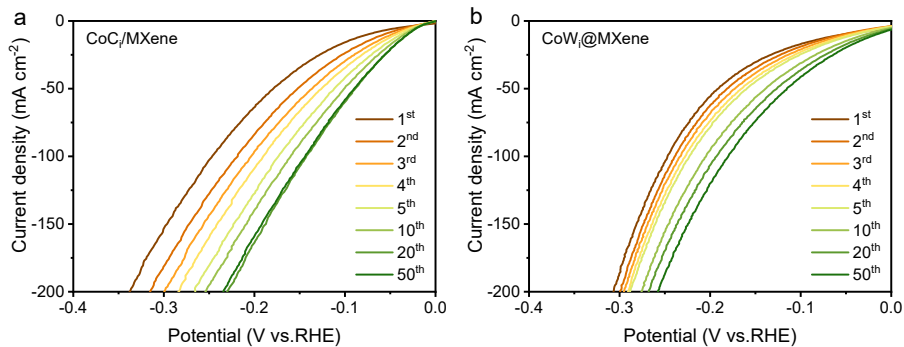
Fig. S39. LVS curves of (a) CoC$_i$/MXene, (b) CoW$_i$/MXene.
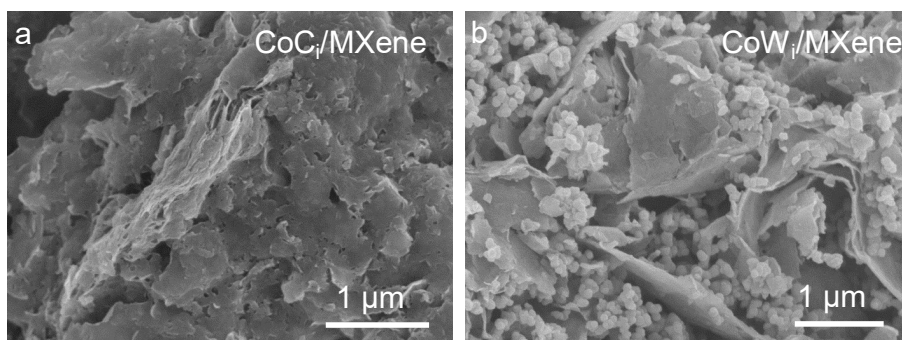
Fig. S40. SEM images of (a) CoC$_i$/MXene and (b) CoW$_i$/MXene.
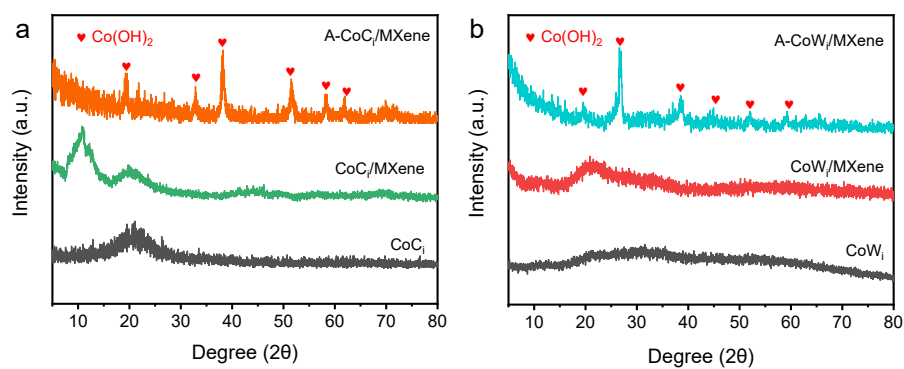
Fig. S41. XRD patterns of (a) CoC$_i$/MXene, (b) CoW$_i$/MXene before and after long-term stability testing in 1 M KOH.
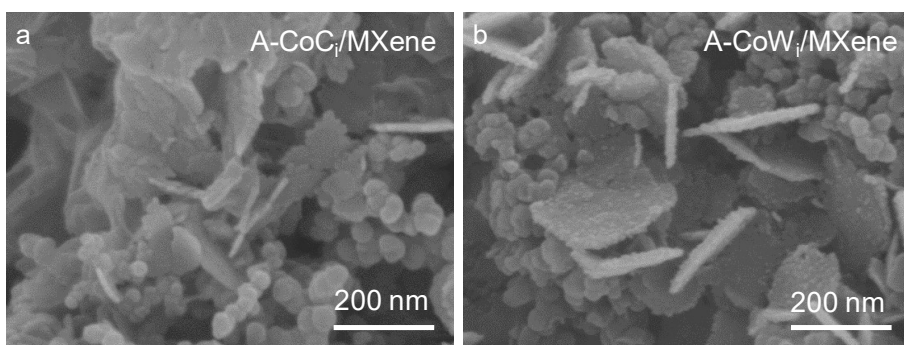
Fig. S42. SEM images of (a) A-CoC$_i$/MXene and (b) A-CoW$_i$/MXene.
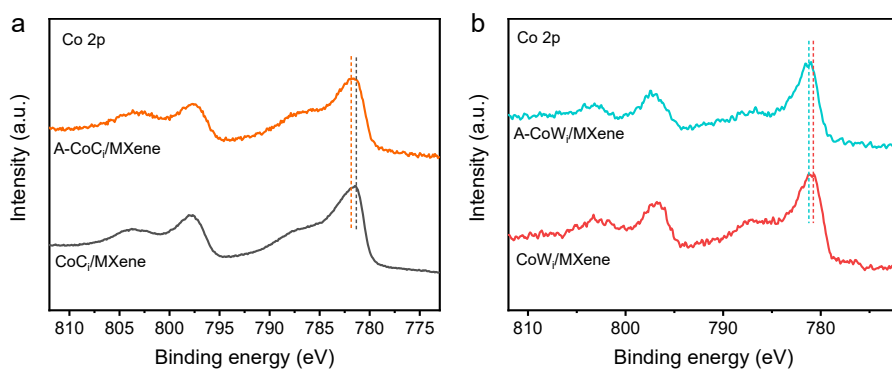
Fig. S43. (a) Co 2p of CoC$_i$/MXene and A-CoC$_i$/MXene. (b) Co 2p of CoW$_i$/MXene and A-CoW$_i$/MXene.
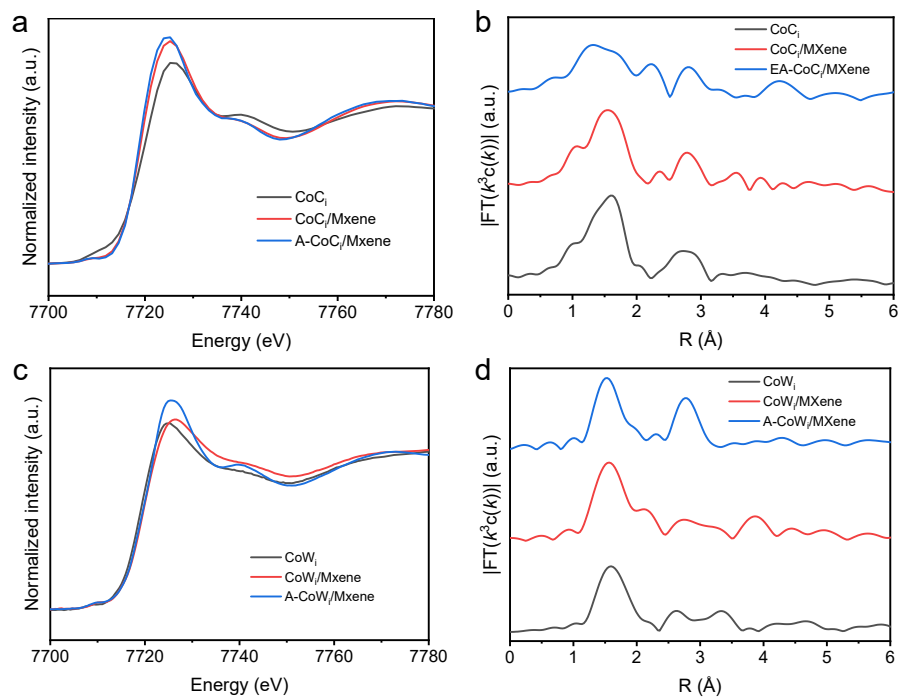
Fig. S44. XAS of (a and b) CoC$_i$/MXene, (c and d) CoW$_i$/MXene.
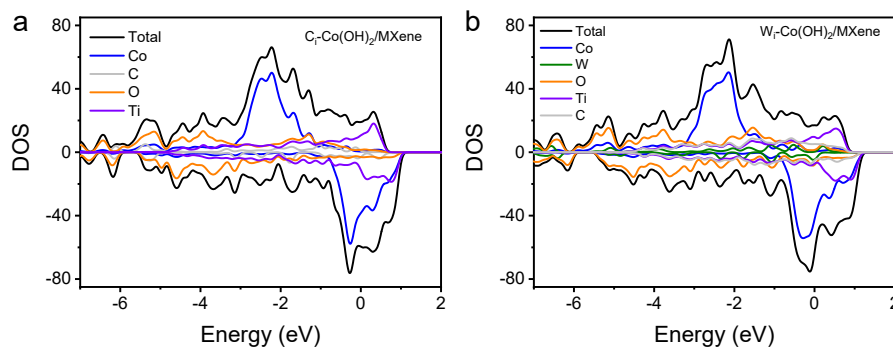
Fig. S45. The projected density of states (PDOS) of (a) CoCi/MXene, (b) CoWi/MXene.
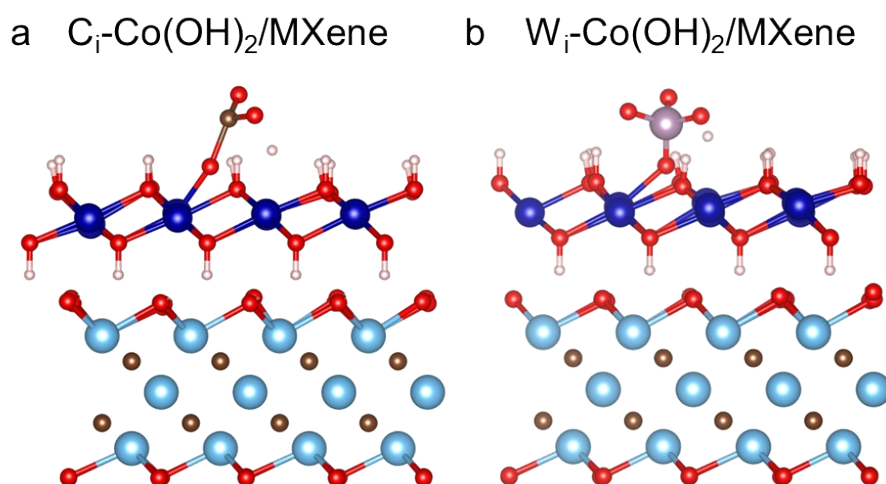
Fig. S46. Chemisorption models of H on the (a) Ci-Co(OH)$_2$/MXene and (b) Wi-Co(OH)$_2$/MXene.
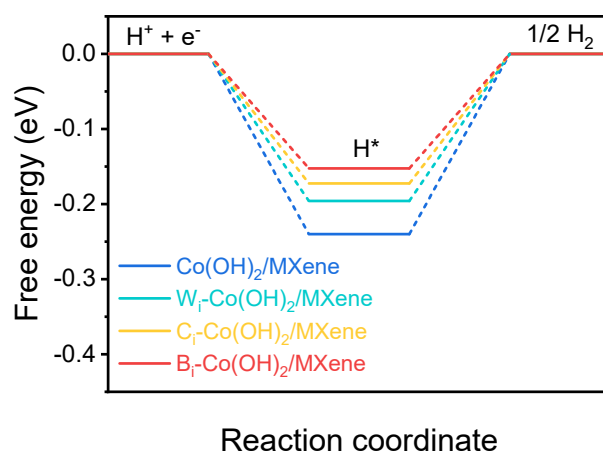
Fig. S47. The Gibbs free energy of H adsorption (ΔG_{H*}) of X-Co(OH)$_2$/MXene (X = B$_i$, C$_i$, and W$_i$).

Supplementary Tables

Table S1. Inductive Coupled Plasma (ICP) results and XPS data of CoBi/MXene.

	ICP (wt%)	XPS (at%)
Co	65.2%	9.2%
Ti	6.4%	2.6%

Table S2. Comparison of the HER activity for a-CoBi/MXene with other activated electrocatalysts.

Pre-catalyst	Activated-catalyst	Overpotential at 10 mA cm^{-2} (mV)	Tafel slope (mV dec^{-1})	Reference
CoB$_i$/MXene	**B$_i$-Co(OH)$_2$/MXene**	**15**	**30.5**	**This work**
Co$_{3-x}$Ni$_x$O$_4$/NF	Co$_y$Ni$_{1-y}$O	57	76.9	ACS Catal., 2021, 11, 8174
NiSe$_2$	NiSe	65	76	ACS Energy Lett., 2020, 5, 2483
CoSe$_{1.26}$P$_{1.42}$	Co(OH)$_2$ and metallic Co	43	90	ACS Energy Lett., 2019, 4, 987
Mo$_2$C-Mo(VI)O$_x$/CC	Mo$_2$C-Mo(IV)O$_x$/CC (1.0 M HClO$_4$)	60	53	Angew. Chem. Int. Ed., 2020, 59, 3544
Ni-BDT NSs	Ni NSs	80	70	Chem, 2017, 3, 122
CoP	CoP and Co(OH)x	100	76	Chem. Sci., 2019, 10, 2019
CoW sulfide	CoO/Co(OH)$_2$+WO$_4$$^{2-}$	189	127	J. Mater. Chem. A, 2021, 9, 11359
TiO$_2$@Co$_2$P$_4$O$_{12}$	metallic Co	81@20	87	J. Mater. Chem. A, 2019, 7, 12457
CoNPs@C	Co(OH)$_2$	58	51	Nano Energy, 2018, 49, 14
NiS$_2$	metallic Ni	67	63	Nano Energy, 2017, 41, 148
Ni$_3$S$_2$@NPC	O$_2$-induced Ni$_3$S$_2$@NPC	91.6 (1M H$_2$SO$_4$)	63.5	Nano Energy, 2017, 36, 85
TiO$_2$@CoCH	Co(OH)$_2$	97@20	80	Nano Energy, 2021, 82, 105732
1T′-MoTe$_2$	distortion of the MoTe$_2$	178 (1M H$_2$SO$_4$)	68	Nat. Commun., 2019, 10, 4916
CoF$_2$	Co(OH)$_2$	54	56	Adv. Sci. 2021, 2103567
Ni$_4$Mo alloy	metal Ni+Mo$_2$O$_7$$^{2-}$	86@100	-	Angew. Chem. Int. Ed. 2021, 60, 7051
MoP@PC	MoP and a few layers of coated graphene	68	41	Nano-Micro Lett., 2021, 13, 215
CoFeO@BP	CoFe phosphide	88	51	Angew. Chem. Int. Ed., 2020, 59, 21106

Table S3. Comparison of the HER activity for A-CoBi/MXene with other non-noble metal-based electrocatalysts in alkaline electrolyte.

Sample	Overpotential (mV) @10 mA cm^{-2}	Overpotential (mV) @500 mA cm^{-2}	References
A-CoBi/MXene	**15**	**180**	**This work**
2H $Nb_{1.35}S_2$	46	247	Nat Mater. 2019, 18, 1309.
$NiMoO_x$/NiMoS	38	186	Nat. Commun. 2020, 11, 5462.
MoS_2/Mo_2C	45	191	Nat. Commun. 2019, 10, 269.
FeP/Ni_2P	85	230	Nat. Commun. 2018, 9, 2551.
CF/VMFP	45	230	Nat. Commun. 2021, 12, 1380.
MoC-Mo_2C-790	98.2	292	Nat. Commun. 2021, 12, 6776.
HC-MoS_2/Mo_2C	280	320	Nat Commun. 2020, 11, 3724.
Co-doped CeO_2	75	240	J. Am. Chem. Soc. 2020, 142, 6461
Ni_2P/NF	85	245	J. Am. Chem. Soc. 2019, 141, 7537
Co-NC-AF	85	272	Adv.Mater. 2021, 33, 2103533.
P-Fe_3O_4/IF	39	212	Adv. Mater. 2019, 31, 1905107.
$Cr_{0.4}Mo_{0.6}B_2$	180	390	Adv. Mater. 2020, 32, 2000855.
Co-Mo_5N_6	19	206	Adv. Energy Mater. 2020, 10, 2002176.
C-$Ni_{1-x}O$/3DPNi	32	220	Adv. Energy Mater. 2020, 10, 2002955.
Ni/FeOOH	38	287	Adv. Energy Mater. 2020, 10, 1904020.
NFN-MOF/NF	87	293	Adv. Energy Mater. 2018, 8, 1801065.
E-Co SAs	59	280	Adv. Funct. Mater. 2021, 31, 2100547.
Pt@Cu-0.3	35	300	Adv. Funct. Mater. 2021, 31, 2105579.
Ni-Mo-B HF	23	329	Adv. Funct. Mater. 2021, 32, 2107308.
PS-Cu	121	750	Adv. Funct. Mater.2022, 2112367.
Ni_2P-CuP_2	51	360	ACS Nano. 2021, 15, 5586-5599.
NiMnOP/NF	81	195	Nano Energy. 2020, 69, 104432.
NiFe-LDH/MXene/NF	132	205	Nano Energy. 2019, 63, 103880.
MFN-MOFs(2:1)/NF	79	234	Nano Energy. 2019, 57, 1–13.
Co_1/PCN	89	N.A.	Nat. Catal. 2018, 2, 134.
CrO_x/Cu–Ni	48	N.A.	Nat. Energy 2018, 4, 107.
W_1Mo_1-NG	67	N.A.	Sci. Adv. 2020, 23, 6586.
NFP/C-3	87	N.A.	Sci. Adv. 2019, 5, 6009.
$Fe(OH)_x$@Cu-MOF NBs	112	N.A.	Sci. Adv. 2021, 7, 580.
PW-Co_3N NWA/NF	41	N.A.	Nat. Commun. 2020, 11, 1853.
Ni–Fe NP	46	N.A.	Nat. Commun. 2019, 10, 5599.

NiCo-SAD-NC	61	N.A.	Nat Commun. 2021, 12, 6766.
3CoMo-Vs	75	N.A.	Nat Commun. 2020, 11, 2253.
$1T_{0.72}$-MoS_2@NiS_2	95	N.A.	Nat Commun. 2021, 12, 5260.
MoC-Mo_2C-790	98.2	N.A.	Nat Commun. 2021, 12, 6776.
LSC/K-$MoSe_2$	128	N.A.	Nat Commun. 2021, 12, 4606.
CuCo-CAT/CC	52	N.A.	Adv. Mater. 2021, 33, 2106781.
CoNi-inf	72	N.A.	Adv. Mater. 2020, 32, 2002857.
Ni/Ni(OH)$_2$	77	N.A.	Adv. Mater. 2020, 32, 1906915.
Ni@N-HCGHF	95	N.A.	Adv. Mater. 2020, 32, 2003313.
MoO_2-FeP@C	103	N.A.	Adv. Mater. 2020, 32, 2000455.
Ni_4Mo	34	N.A.	Angew. Chem. Int. Ed. 2021, 60, 7051.
Ni_3N-Co_3N PNAs/NF	43	N.A.	Angew. Chem. Int. Ed. 2021, 60, 5984.
S-$NiFe_2O_4$	61	N.A.	Angew. Chem. Int. Ed. 2021, 60, 14117
Co-MoS_2@CoS_2	76	N.A.	Angew. Chem. Int. Ed. 2022, 61, 202114899.
CoFeO@BP	88	N.A.	Angew. Chem. Int. Ed. 2020, 59, 21106.
P-MoP/Mo_2N	89	N.A.	Angew. Chem. Int. Ed. 2021, 60, 6673.
CoP_x@CNS	91	N.A.	Angew. Chem. Int. Ed. 2020, 59, 21360.
N-c-$CoSe_2$	98	N.A.	Angew. Chem. Int. Ed. 2021, 60, 21575.
S-$Co_{0.85}$Se-1	108	N.A.	Angew. Chem. Int. Ed. 2021, 60, 12360.
2D meso-Mo_2C/Mo_2N	110	N.A.	Angew. Chem. Int. Ed. 2022, 61, 202112298.
NiP_2-650	134	N.A.	Angew. Chem. Int. Ed. 2021, 60, 259.
Co-MoS_2	137	N.A.	Angew. Chem. Int. Ed. 2021, 60, 7251.
$Co_{0.9}Ni_{0.1}$Se	185.7	N.A.	Angew. Chem. Int. Ed. 2020, 59, 22743.

Table S4. Comparison of the HER activity for A-CoBi/MXene with other noble metal-based electrocatalysts in alkaline electrolyte.

Sample	Overpotential (mV) @10 mA cm^{-2}	Tafel slope (mV dec^{-1})	References
A-CoBi/MXene	**15**	**30.5**	**This work**
Pt/MgO	39	39	Nat. Commun. 2022, 13, 2024
Cl-Pt/LDH	25.2	34.33	Nat. Commun. 2022, 13, 6875
Pt-ACs/CoNC	40	N.A.	Nat. Commun. 2022, 13, 2430
V$_O$-Ru/HfO$_2$-OP	39	29	Nat. Commun. 2022, 13, 1270
Ru NPs/NC-900	19	40	J. Am. Chem. Soc. 2022, 144, 19619
Ru-a-CoNi	15	34	Angew. Chem. Int. Ed. 2022, 61, e202114160
Ru/P-TiO$_2$	27	28.3	Angew. Chem.Int. Ed. 2022, 61, e202212196
Pt$_{doped}$@WC$_x$	20	15	Adv.Mater. 2022, 34, 2206368
Pt$_{SA}$-Mn$_3$O$_4$	24	54	Energy Environ. Sci. 2022, 15, 4592-4600
D-NiO-Pt	20	31.1	Adv. Energy Mater. 2022, 12, 2200434

Table S5. FEFF fitting parameters for Co–K edge of CoB$_i$/MXene in situ XAS data.

Condition	path	CN[a]	σ^2 (Å)^2	ΔE (eV)	R (Å)	R factor
OCV	Co–O	5.4(3)	0.003(5)	−4.1(2)	1.92(2)	0.007
	Co–O–Co	4.0(1)	0.002(5)	−4.1(2)	2.82(2)	
−0.05 V	Co–O	5.2(1)	0.002(1)	−6.7(1)	1.88(1)	0.010
	Co–O–Co	5.0(2)	0.004(2)	−6.7(1)	2.83(3)	
−0.10 V	Co–O	6.0(4)	0.001(3)	−2.2(1)	1.90(1)	0.015
	Co–O–Co	5.0(1)	0.002(2)	−2.2(1)	2.86(2)	
−0.15 V	Co–O	7.2(3)	0.003(2)	−3.6(5)	1.88(5)	0.013
	Co–O–Co	5.8(4)	0.001(1)	−3.6(5)	2.84(1)	
−0.20 V	Co–O	7.8(2)	0.002(1)	−1.9(4)	1.89(2)	0.010
	Co–O–Co	5.6(1)	0.003(3)	−1.9(4)	2.84(3)	

[a]Coordination number.

Table S6. FEFF fitting parameters for Co–K edge of CoB$_i$ in situ XAS data.

Condition	path	CN[a]	σ^2 (Å)^2	ΔE (eV)	R (Å)	R factor
OCV	Co–O	4.9(2)	0.005(1)	−4.1(4)	1.90(2)	0.014
	Co–O–Co	3.2(1)	0.002(2)	−4.1(4)	2.84(2)	
−0.05 V	Co–O	5.1(3)	0.002(1)	−1.5(4)	1.89(7)	0.010
	Co–O–Co	5.1(4)	0.001(4)	−1.5(4)	2.83(6)	
−0.10 V	Co–O	5.6(2)	0.005(1)	−5.1(5)	1.90(1)	0.008
	Co–O–Co	5.8(4)	0.002(3)	−5.1(5)	2.84(2)	
−0.15 V	Co–O	5.8(5)	0.005(1)	−5.0(4)	1.92(1)	0.010
	Co–O–Co	5.8(6)	0.003(2)	−5.0(4)	2.84(2)	
−0.20 V	Co–O	6.0(3)	0.001(2)	−3.5(3)	1.93(2)	0.012
	Co–O–Co	5.8(2)	0.002(5)	−3.5(3)	2.86(5)	

[a]Coordination number.

Table S7. Comparison of different calculated energies on the prepared catalysts.

	d-band center (eV)	ΔG_{H*} (eV)	$E_{ads}(H_2O*)$ (eV)	Kinetic barrier (eV)
CoB_i	−1.496	−0.69713	−0.574	0.85261
CoB_i/MXene	−1.305	−0.41334	−1.031	0.76135
$Co(OH)_2$/MXene	−1.139	−0.36545	−1.566	0.52659
B_i-$Co(OH)_2$/MXene	−0.965	−0.20436	−1.819	0.41065